A Fast Soft Robotic Laser Sweeping System Using Data-Driven Modeling Approach

Kui Wang ⓘ, Xiaomei Wang ⓘ, Justin Di-Lang Ho ⓘ, Ge Fang ⓘ, Bohao Zhu ⓘ, Rongying Xie ⓘ, Yun-Hui Liu ⓘ, *Fellow, IEEE*, Kwok Wai Samuel Au, Jason Ying-Kuen Chan ⓘ, and Ka-Wai Kwok ⓘ, *Senior Member, IEEE*

Abstract— Soft robots have great potential in surgical applications due to their compliance and adaptability to their environment. However, their flexibility and nonlinearity bring challenges for precise modeling, sensing, and control, especially in constrained cavities. In this article, a simple, compact two-segment soft robot for flexible laser ablation is proposed. The proximal hydraulic-driven segment can offer omnidirectional bending so as to navigate toward lesions. The distal segment driven by tendons enables precise, fast steering of laser collimator for laser sweeping on lesion targets. The dynamics of such mechanical steering motion can be enhanced with a metal spring backbone integrated along the collimator, thus facilitating the control with certain linearity and responsiveness. A soft robot modeling and control scheme based on Koopman operators is proposed. We also design a disturbance observer so as to incorporate the controller feedback with real-time fiber optic shape sensing. Experimental validation is conducted on simulated or *ex-vivo* laser ablation tasks, thus evaluating our control strategies in laser path following across various contours/patterns. As a result, such a simple compact laser manipulation can perform up to 6 Hz sweeping with precision of path following errors below 1 mm. Such modeling and control scheme could also be used on an endoscopic laser ablation robot with unsymmetric mechanism driven by two tendons.

Index Terms—Fiber optic shape sensing, Koopman operator, laser sweeping, soft robot modeling and control.

Kui Wang, Justin Di-Lang Ho, Ge Fang, Bohao Zhu, and Ka-Wai Kwok are with the Department of Mechanical Engineering, The University of Hong Kong, Hong Kong (e-mail: kuiwang@connect.hku.hk; jdlho@connect.hku.hk; fangge@hku.hk; zhubohao9374@gmail.com; kwokkw@hku.hk).

Xiaomei Wang and Rongying Xie are with the Department of Mechanical Engineering, The University of Hong Kong, Hong Kong, and also with the Multiscale Medical Robotics Center, Hong Kong (e-mail: wangxmei@connect.hku.hk; ryxie@connect.hku.hk).

Yun-Hui Liu is with the Department of Mechanical and Automation Engineering, The Chinese University of Hong Kong, Hong Kong (e-mail: yhliu@mae.cuhk.edu.hk).

Kwok Wai Samuel Au is with the Department of Mechanical and Automation Engineering, The Chinese University of Hong Kong, Hong Kong, and also with the Multiscale Medical Robotics Center, Hong Kong (e-mail: samuelau@cuhk.edu.hk).

Jason Ying-Kuen Chan is with the Department of Otorhinolaryngology, Head and Neck Surgery, The Chinese University of Hong Kong, Hong Kong (e-mail: jasonchan@ent.cuhk.edu.hk).

This article has supplementary material provided by the authors and color versions of one or more figures available at https://doi.org/10.1109/TRO.2023.3262118.

Digital Object Identifier 10.1109/TRO.2023.3262118

I. INTRODUCTION

FLEXIBLE continuum robots have demonstrated numerous advantages and wide applications in minimally invasive surgery in recent years [1], [2], [3], [4]. Applied as instruments such as endoscopes and cardiac catheters, they can perform large and complex deformations through flexible actuation methods including cables and pressurized fluid [5], [6], while being capable of meeting high requirements for size and control accuracy [7], [8]. Among surgical applications, noncontact laser ablation is a promising area that can leverage the enhanced access and dexterity provided by continuum robots. Laser ablation is performed by projecting a high-power laser beam onto tissue, creating an incision or ablation effect [9], [10], [11]. It is associated with reduced postoperative pain and shortened recovery time [10]. However, to achieve precise treatment margin and minimize damage to healthy tissue, the laser probes need to be precisely and frequently steered during the ablation process. Studies have shown that the speed of laser-fiber sweeping affects tissue ablation efficiency [12], [13], which indicates a need for not only precise motion, but also motion with adequate velocity.

In surgical applications, various laser manipulation instruments or robotic platforms have been proposed [14], [15]. In a conventional setup for transoral laser microsurgery, surgeons manually manipulate a beam-splitter mirror that projects the laser beam at the targeted lesions [16]. To improve the laser aiming precision and efficiency, motorization of external manipulators was introduced [17]. Motorized laser scanners (e.g., Lumenis AcuBlade) that allow preprogrammed scan patterns are commercially available, providing improved laser incision quality [16]. However, these laser systems generally depend on "line-of-sight" projection from an external manipulator to the surgical site, often resulting in the patient being positioned with significant neck extension. The long working distance also causes a lever effect on the laser beam, which can amplify inaccuracies in laser steering and require large external suspension arms.

As an alternative, flexible optical fiber lasers allow delivery of the laser directly to the target area without direct line of sight. This presents the opportunity for flexible, yet dexterous surgical robotic devices to control the laser fiber within the body [9]. For example, Acemoglu et al. [18] proposed a flexible robotic laser scanner, which used four electromagnetic (EM) coils and a permanent magnet to manipulate a laser fiber, however, the projection workspace of laser spot was restricted to a 5×5 mm

square. Patel et al. [19] designed a laser scalpel using a Risley prism beam steering mechanism, which could be mounted on a modified laryngoscope for noncontact laser surgery. However, the 5-cm long rigid design at the distal tip limited its application in narrow and confined anatomical spaces. Fang et al. [20] proposed a magnetic resonance safe endoscopic robot system that provided dexterous and flexible access to lesions in the confined oral cavities within the magnetic resonance imaging bore. However, the laser steering speed was limited as the soft chambers and cylinders were driven via 10-m long tubes. There were few prior arts of gimbal mechanism, e.g., Hu et al. [21] proposed for the pan-tilt movement in endoscopic settings, somehow as known as universal joint, such a mechanism was usually used to actuate or manipulate an entire robot segment/link containing an endoscopic camera unit. The gimbal design would usually encounter challenges in further miniaturization (e.g., $\varnothing < 9$ mm). Overall, there remains a need for flexible and compact robotic laser steering systems which enable both accurate and fast laser ablation.

The inherent compliance and flexibility of soft robotics presents an interesting proposition for its application in surgery, particular in narrow natural orifices. However, a persistent challenge with flexible robotic systems in general is how to balance the *tradeoff* between precision and structural flexibility. To achieve reliable control, similarly flexible sensing technology should be incorporated to obtain real-time feedback. However, due to the deformable nature of soft robots, accurately sensing their morphology still remains a challenge [22], [23]. EM tracking systems with discrete positional sensors are widely used to localize and track continuum robot configurations within the human body, accredited to small size and high sensing accuracy of the tracking markers [24]. However, the sensing volume of the EM-based devices can be limited and the sensing error is also highly sensitive to ferromagnetic objects [25], [26]. Optoelectronic sensing technology has emerged as a category of flexible sensor in which strain/force is measured through detecting optical signals [27], [28]. For example, strain sensing using optical fiber Bragg gratings (FBG) has drawn attention in the surgical field because of its thin size, high sensitivity, and biocompatibility. Compared to EM sensors, FBG-based sensors have several advantages, such as being inherently deformable and easily providing multiple sensors along one fiber [29], [30]. FBG fibers with single cores have been integrated with instruments and soft manipulators in a variety of ways, such as through multiple fibers aligned in parallel along a instrument's center axis [31], [32], or by a single helically wound fiber [33], [34]. A preferable alternative is FBG fiber with multiple cores built directly into a single strand, allowing for simplified integration and the ability to directly measure the fiber's shape. This is achievable through optical frequency-domain reflectometry (OFDR) technology, which also enables pseudocontinuous strain sensing along each of the fiber cores [35], [36].

Alongside challenges in sensing, the modeling and control of flexible continuum robots poses problems due to the inherent nonlinearity of their actuation [37]. Compared with analytical models, data-driven methods are a powerful tool for soft robots as they rely on observing the system behavior rather than on simplified assumptions of geometric structure or component material properties [38]. Wang et al. [39] presented an example of an endoscopic soft robot prototype that was helically wrapped with an FBG fiber and leverages learning-based motion estimation. The learning method alleviated the demanding of assembly accuracy and could provide accurate control when fused with visual-strain sensing feedback. However, the update frequency of these learning-based solutions is usually limited due to higher computational demand, thus hampering the capability of fast dynamic motion compensation. Besides, these learning-based approaches are difficult to be cooperated with existing control strategies, as they could only provide "black-box" mappings rather than analytical solutions [40]. To this end, Koopman operator theory is a type of data-driven approaches, which could circumvent simplified physical assumptions and complex numerical analysis with data-driven identification methods [40], [41]. The analytical solutions can be initialized and approximated for a nonlinear system with equivalent linear representation [42]. Therefore, it could yield explicit numerical models [43], and be cooperated with many existing model-based control strategies. Besides, disturbance rejection is important in controller design, especially for surgical applications [44]. For measurable disturbances, feed-forward strategies can be used to reduce or eliminate the influence. However, in most situations, the internal or external disturbances cannot be directly measured. A promising solution to this problem is to estimate the disturbance based on measurable variables, followed by control strategies that can reduce the influence of disturbance [45].

In this article, we develop a modeling and control scheme with the aim at achieving fast, precise laser steering implemented by a flexible, compact continuum robot structure. Precise robot control is achieved through real-time multicore FBG shape sensing, Koopman-based robot modeling, and a disturbance-observer-based controller. Lab-based laser ablation tasks are also conducted to evaluate the robotic system. The motivation of this article is to propose a compact soft robot with high compliance and fast laser sweeping capability, which can be implemented in narrow orifices for laser surgery, such as transoral laser microsurgery. The key work contributions are listed as follows.

1) Design of a compact two-segment soft robot with fast laser sweeping capability. A proximal hydraulic-driven segment can provide omnidirectional endoscopic navigation of the distal segment that is actuated by tendons for precise and fast laser sweeping.
2) Development of Koopman-based data-driven models, which could provide linear presentations of the nonlinear property for both the hydraulic-driven and tendon-driven mechanisms.
3) Design of a disturbance-observer-based controller, where the control loop can be closed by real-time shape sensing feedback of a multiple-core FBG passing through the two robot segments.

II. METHOD

In this article, the design of the two-segment soft robotic system is presented. To enable accurate and reliable laser ablation in
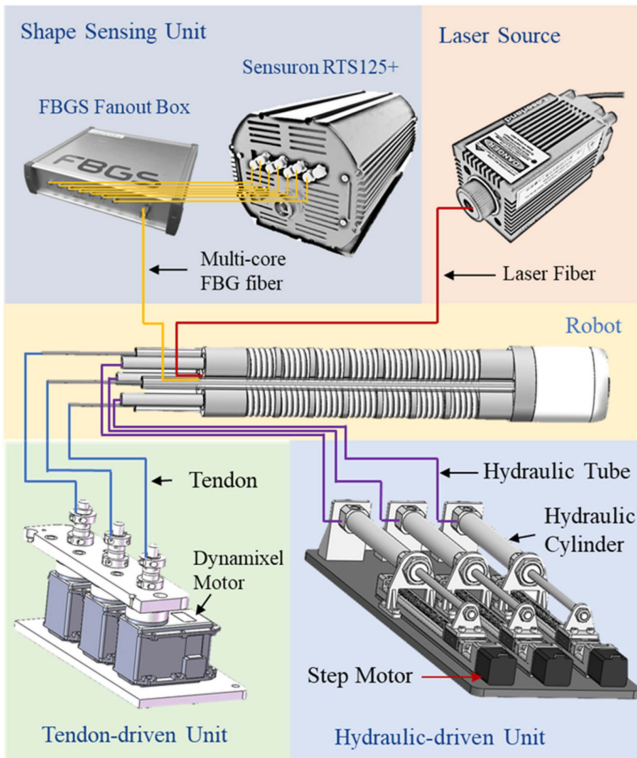
Fig. 1. Diagram showing the architecture of the robotic laser ablation system. The proximal segment is driven by three hydraulic cylinders which are connected to a step motor, respectively. The distal segment is driven by three tendons which are wrapped on rollers and controlled by three Dynamixel motors. The multicore FBG fiber and laser fiber are both inserted into the central channel of the robot, connected to an interrogator and laser source, respectively.
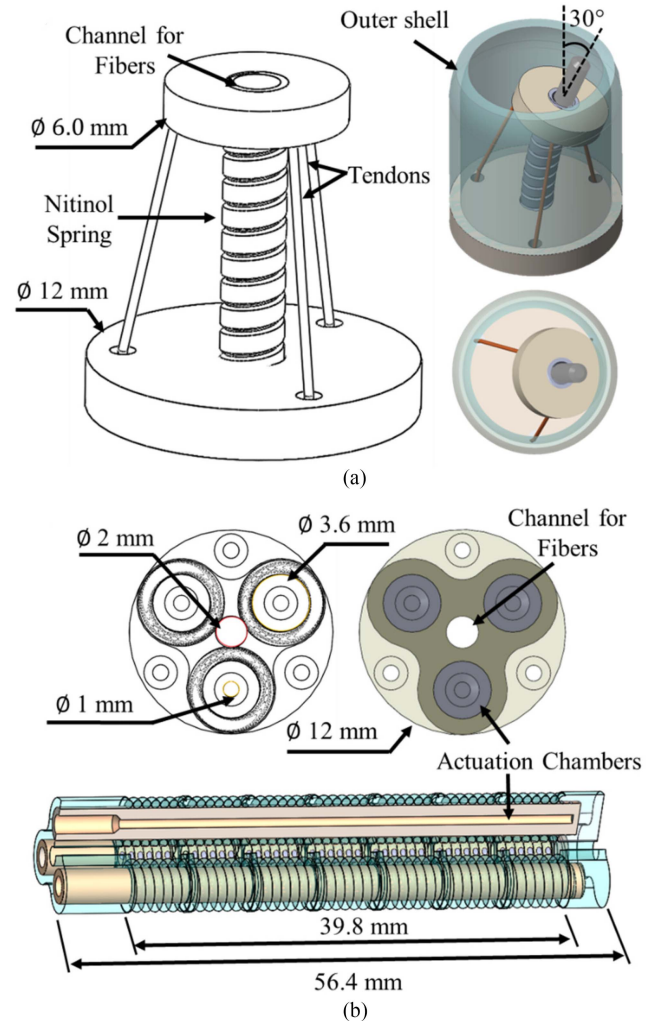

Fig. 2. Components of the two-segment continuum robot. (a) Conical design of the distal tendon-driven segment. The manipulator is driven by three PE cables, with a metal spring as the backbone. An outer shell could protect the bending structure from external disturbances. (b) Proximal hydraulic-driven segment for large deformation. The active bending segment is comprised of three soft chambers with individual spring reinforcement constraints.

a narrow and constrained environment, the robot should have a compact design without sacrificing its manipulation capabilities. The design, modeling, and control of the soft robotic system is detailed in this section. The overall hardware configuration is shown in Fig. 1, including the tendon-driven unit, the hydraulic-driven unit, the shape sensing unit, the laser source for ablation, and the two-segment robot. Three servo motors (Dynamixel MX-64 AT) were used to adjust the tendon length, thus steering the laser lens in the distal segment. Three step motors (57BYG250-80) driving linear motion of the cylinder piston for hydraulic actuation of the three soft chambers. Besides, a multicore FBG fiber was used and connected along the central channel throughout the two robot segments to the fiber optic interrogator device (Sensuron, RTS125+). The fiber multiple cores were split into separate channels of the fanout box (FBGS International). The patch cables were then connected to the interrogator through broadband reflectors. The interrogator could provide a laser source transferred to the optical FBGs and process the spectral data in real time. The fiber together with an outer sheath (PTFE, ID Ø0.3 mm, OD Ø0.6 mm) is inserted in the central channel of the robot and fixed at the distal end. Another optic fiber with gradient-index (GRIN) lens was used for laser ablation powered by another external laser source (808 nm, 3 W)."

A. Robot Prototype

The robot's two segments are both able to perform omnidirectional bending, with the proximal hydraulic-driven segment designed for large bending, and the distal tendon-driven segment for fast laser scanning within a smaller angular range. The relatively large bending range of the hydraulic-driven segment is designed with the purpose of adjusting the laser orientation roughly toward the target where fine, but fast laser steering can then be performed by the tendon-driven segment. The laser manipulator, namely the distal segment [Fig. 2(a)], incorporates three tendons spaced circumferentially about a flexible backbone with a total length of 12 mm, offering panning and tilting of the laser collimator. Polyethylene (PE) tendons (Ø 0.5 mm) were selected in this article due to their low stretchability and high durability. Also, compared with metal wires, PE is softer with

little shape memory effect, which would reduce the buckling effect. The backbone is a metal spring fabricated from a nitinol tube using laser cutting. The central channel of the segment is reserved for a laser ablation fiber, which has a rigid collimator on the tip as well as the multicore FBG fiber for shape reconstruction. A rigid outer shell (Ø 12 mm) is incorporated to prevent the laser beam steering from external disturbances, such as contact with tissue. Note that the outer shell would not affect the bending of soft manipulator. To enable a large ablation region, a smaller disc (Ø 6 mm) is used in the conical design for larger steering angle ($\sim \pm 30°$) inside the outer shell (Fig. 2).

The workspace can be roughly estimated with an analytical model using constant curvature (CC) theory [46]. This design enables a scanning area of 20×20 mm^2 at a 15 mm projection distance. The usage of the nitinol spring as the backbone allows the stiffness of the tendon-driven segment to be reduced in comparison to the hydraulic-driven segment. The stiffness difference between the two segments can ensure that the tendon-driven segment could work independently, i.e., when the distal segment is actuated, the hydraulic segment would not undergo deformation or vibration.

In our application cases, the manipulator is expected to provide flexible laser steering in narrow orifices while maintaining the camera pose/view stable or still. This requires an omnidirectional bending mechanism that has to be sufficiently small to accommodate inside a cap or shell. The proposed spring-tendon mechanism can fulfill such small form factors required, and also protect the fiber from any damage due to its sharp bending as which would be occurred in gimbal setting. Furthermore, it is very challenging to incorporate an elastic property into the compact gimbal, which is of importance to reducing the drawback of any tendon slackness commonly found in tendon-driven mechanisms. The introduced elasticity would help minimize the mechanical transmission latency and backlash, enhancing the overall dynamic response, hence the control performance. Not applying any pretension/load on the tendons, in our tendon-driven structure, multiple closed-coil spring partitions could be just simply enclosed along the laser fiber, avoiding its sharp bending to damage.

The mechanism of the hydraulic segment consists of three independent elastic actuation chambers, which are located 120° apart in a symmetric triangular configuration. The hydraulic segment is fabricated with three-dimensional (3-D) printing (Objet 350, Stratasys), which could provide hybrid printing of soft and rigid materials. Reinforced springs made from stiff materials are directly applied to each soft chamber through 3-D printing. With the spring reinforcement constraint, the soft hydraulic chambers could deform with lower hysteresis and higher stiffness while improving resistance to rupturing during pressurization. This long hydraulic-driven segment [Fig. 2(b)] comprises of three spring reinforced chambers each with outer diameter of 2 mm and a total length of 56.4 mm, enabling coarse navigation toward the region of interest prior to more precise laser steering provided by the distal tendon-driven segment. There is a central channel reserved for laser fiber and shape sensing fiber.

B. Shape Sensing With Multicore Optical Fiber

Fiber-optic shape sensing technologies using FBGs have drawn attention for their ability to measure the configuration of flexible instruments in a small package. FBG fibers have excellent multiplexing capabilities within thin, submillimeter diameters, where a series of sensing gratings can be written on one fiber without changing the fiber diameter [33]. Also, the high flexibility of the optical fiber allows it to be integrated with delicate devices with minimal effect on the instrument stiffness. These distinctive advantages of FBG fibers have prompted their employment in many applications, including shape sensing of steerable interventional needles [47], [48], navigation of medical devices [49], and force sensing of surgical instruments [50], [51]. Another advantage is that it can achieve real-time shape reconstruction with high updating frequency (>100 Hz).

Fiber with multiple cores containing FBGs could further improve the sensing density and enable 3-D shape sensing of the fiber's own configuration [52]. For multicore fibers, its own configuration can be uniquely estimated by strains measured along each core, where different cores will measure different strains (tension or compression) under bending. The bending direction and radius (curvature) can be uniquely determined by comparing the amplitude and phase of each strain curve. For multicore fiber, there are two types of 3-D curvature calculation methods commonly used. One approach is utilizing the piecewise constant curvature (PCC) model with the assumption that each small section between strain measurements is bent in CC. The model works by calculating the discrete bending radius and direction for each segment and sums them to obtain the 3-D fiber shape [53]. Another method is utilizing the Frenet–Serret formulas to define 3-D curves, taking the torsion effect into account [54], [55]. In this article, the PCC method was selected in consideration of its relative simplicity. Additionally, the length of the fiber/robot (~ 60 mm for the hydraulic-driven segment and ~ 16 mm for the tendon-driven segment) used in this article is relatively short, reducing the need for torsion compensation.

An independent demonstration of shape reconstruction with multicore OFDR FBG fiber is shown in Fig. 3, where the fiber was manually deformed into various curves. A ~ 300 mm sensing length was used, with a PTFE sheath protecting it from outer force disturbance and to reduce friction. The torsion of the fiber may contribute to the reconstruction error, which would induce strain response for each core and bring noise into the reconstruction algorithm. This error is related to sensing length and the fabrication accuracy. Once the fiber is tightly fixed with small initial torsion, the reconstruction error can be substantially reduced.

To validate the FBG shape sensing performance of the multicore fiber, a fixed curvature test was conducted on the bending curvature templates, as shown in Fig. 4. The templates were 3-D printed with fixed curvature grooves of 2.5 mm width, which are approximately equal to the outer diameter of outer tube. The tube was placed into the template grooves for measuring its 3-D curvature. The bending angles of the curved section are from 0° to 120° on one side, and from 0° to 60° for the "S" shape. The length of the CC arc section is 78.5 mm. The shape of the
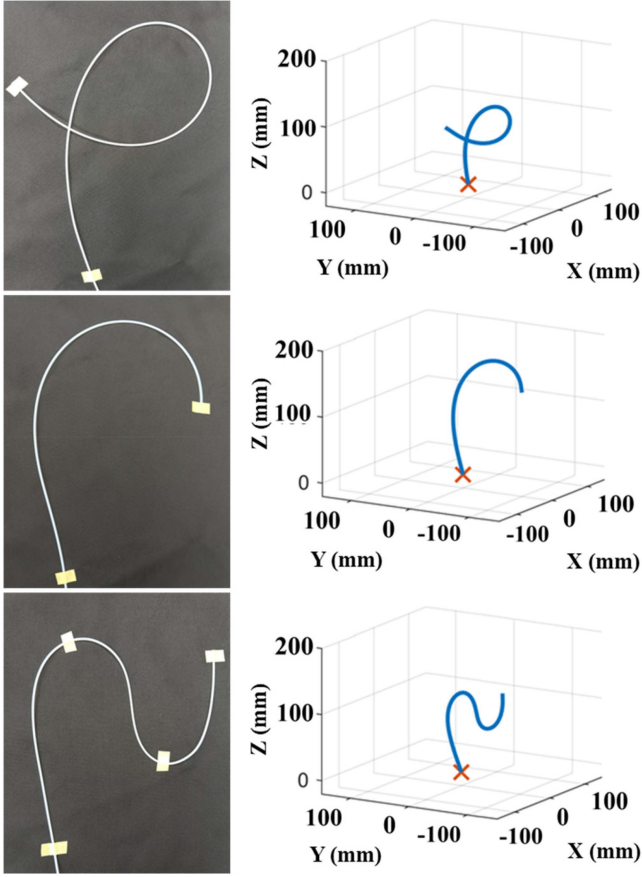
Fig. 3. Shape reconstruction for the multicore fiber in various curvature configurations. The fiber length used in the test was about 300 mm and was protected with a PTFE sheath. The fiber was deformed into different curves (left column) with the corresponding shape reconstruction (right column).
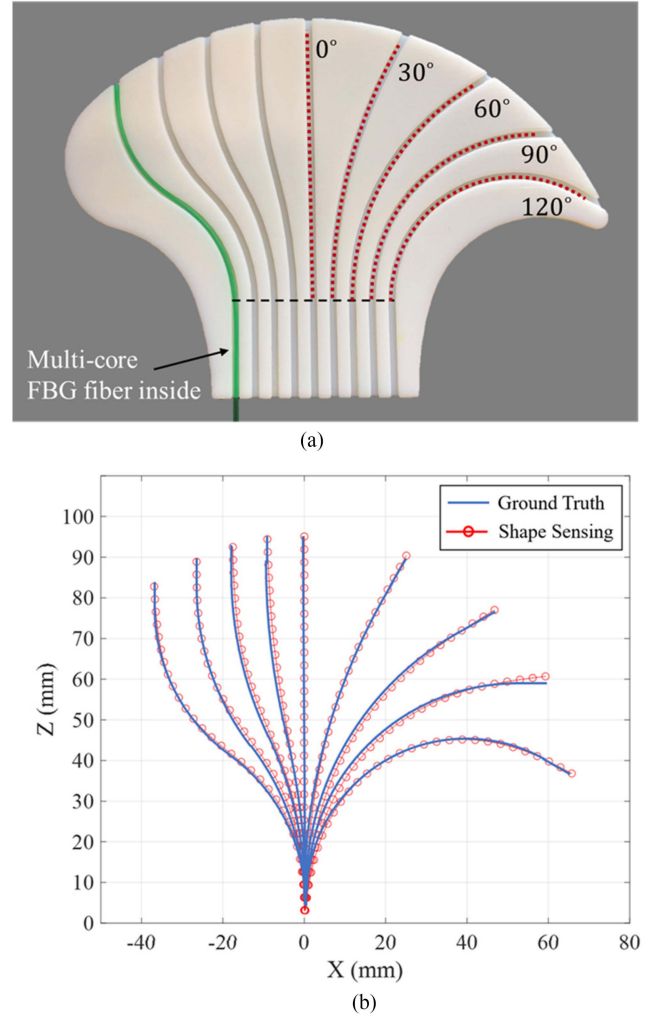

Fig. 4. Shape sensing accuracy test with curvature template. (a) Bending curvature templates used to evaluate the shape sensing performance of the multicore FBG fiber. Eight curvatures are included at each bending direction, with an absolute value from 0° to 120°. (b) Reconstruction shapes compared with the ground truth curves. The starting positions are all aligned at (0, 0).

tube was reconstructed by three cores in the fiber with each core containing 25 FBG segments. For each measurement, the location of first FBG segment was aligned to the start position of the CC arcs. The reconstructed 3-D curvature was obtained by taking average of 20 consecutive data captures for the entire sensing section. In terms of the distal segment, a short length of the fiber ($\sim$12 mm) was used for shape sensing, where the sensing error would be proportionally reduced and meet the clinical requirements on laser spot targeting (<1 mm) [56].

C. Linear Modeling Built on Koopman Operator

Soft robots, unlike their rigid counterparts, usually have infinite degrees of freedom due to their continuously bending structure. Their nonlinearity creates challenges when using traditional analytical methods, such as PCC or Cosserat rod theory. Linearization of nonlinear systems is a useful way to solve the modeling problem of soft robots. Among these linearization techniques, the Koopman-based approach could convert a nonlinear system into an equivalent linear system. The linearization method makes it possible to linearize the system globally, rather than just preserving the stability near equilibrium points. However, like most data-driven methods, the accuracy

of Koopman-based models highly depends on the data quality and quantity. Due to their high compliance, soft robots tend to have smaller physical impact on their surroundings than rigid robots. This in turn allows safe and automatic collection of large amounts of training data, further allowing a wide range of operating conditions.

With the input–output datasets obtained, a linear representation of the nonlinear dynamic system could be identified with the Koopman-based method [40]

$$\dot{x}(t) = F(x(t)) \tag{1}$$

where $x(t) \in X$ represents the system state ($t > 0$), with initial condition x_0 at time 0. F is a differentiable function, and ϕ_t is denoted as the solution to (1) at time t.

The finite-dimensional system state $x(t)$ can be lifted to an infinite-dimensional space $\mathcal{F}$ which includes all continuous real-valued functions ($X \subset \mathbb{R}^n$). Functions in $\mathcal{F}$ are denoted as observables, and the solution can be characterized by the

Koopman operator $\mathbf{\Omega}_t$. For any $t \geq 0$, there is

$$\mathbf{\Omega}_t f = f \circ \phi_t. \tag{2}$$

The symbol $\circ$ means function composition and $\mathbf{\Omega}_t$ is a linear operator, while the system (1) can be linear or nonlinear. Therefore, the Koopman operator can provide a linear expression of a nonlinear system with infinite-dimensional observables [32].

1) Linear Model Identification: In application, the Koopman operator cannot be described by a finite-dimensional matrix due to its infinite dimension. To solve this problem, a modified extended dynamic mode decomposition algorithm is usually utilized to reduce the dimension [57], [58], where a finite-dimensional approximation can be identified by linearly regressing the observed data.

Assume $\overline{\mathcal{F}}$ is the subspace of $\mathcal{F}$, which is spanned by $N(> n)$ independent basis functions $\{\psi_i : \mathbb{R}^n \to \mathbb{R}\}_{i=1}^N$. For convenience, the first n basis functions are set as follows:

$$\psi_i(\mathbf{x}) = x_i \tag{3}$$

where x_i is the ith element of $\mathbf{x}$, and the *lifting* function can be expressed as follows:

$$\boldsymbol{\psi}(\mathbf{x}) := [x_1 \cdots x_n \psi_{n+1}(\mathbf{x}) \cdots \psi_N(\mathbf{x})]^T. \tag{4}$$

The best approximation of $\mathbf{\Omega}_t$ in the L^2-norm sense is as follows [59]:

$$\bar{\mathbf{\Omega}}_t = \left(\boldsymbol{\psi}^T(\mathbf{x})\right)^\dagger (\boldsymbol{\psi} \circ \phi_t(\mathbf{x}))^T \tag{5}$$

where the superscript $\dagger$ indicates the Moore–Penrose pseudoinverse.

For real application in control systems, state measurements are discretized in the form of input–output pairs $(\mathbf{a}[k], \mathbf{b}[k])$ for $k \in \{1, \ldots, K\}$:

$$\mathbf{a}[k] = \mathbf{x}[k] \tag{6}$$

$$\mathbf{b}[k] = \phi_{T_s}(\mathbf{x}[k]) + \boldsymbol{\sigma}[k] \tag{7}$$

where $\mathbf{x}[k]$ is the kth measured state, $\boldsymbol{\sigma}[k]$ represents the noise, and T_s indicates the sampling period. All the data pairs are lifted with (4) and form into the following $K \times N$ matrices:

$$\mathbf{\Psi}_a := \begin{bmatrix} \boldsymbol{\psi}(\mathbf{a}[1])^T \\ \vdots \\ \boldsymbol{\psi}(\mathbf{a}[K])^T \end{bmatrix}, \mathbf{\Psi}_b := \begin{bmatrix} \boldsymbol{\psi}(\mathbf{b}[1])^T \\ \vdots \\ \boldsymbol{\psi}(\mathbf{b}[K])^T \end{bmatrix}. \tag{8}$$

Following from (5), $\bar{\mathbf{\Omega}}_{T_s}$ is thus determined upon the least-squares method to fit the observed data

$$\bar{\mathbf{\Omega}}_{T_s} := \mathbf{\Psi}_a^\dagger \mathbf{\Psi}_b. \tag{9}$$

For dynamic systems with inputs, the Koopman operator is utilized to yield discrete linear models with the following form:

$$\mathbf{z}[j+1] = \mathbf{A}z[j] + \mathbf{B}\mathbf{u}[j]$$
$$\mathbf{x}[j] = \mathbf{C}\mathbf{z}[j] \tag{10}$$

for each $j \in \mathbb{N}$, where $\mathbf{x}[0]$ is the initial state, $\mathbf{z}[0] = \boldsymbol{\psi}(\mathbf{x}[0])$ is the corresponding lifted state, $\mathbf{u}[j] \in \mathbb{R}^m$ is the system input at step j, and $\mathbf{C}$ is a projection matrix from lifted state space onto the robot state space.

A linear model in form of (10) can be obtained using the system identification approach, with the following lifted data pairs:

$$\boldsymbol{\alpha}[k] = \begin{bmatrix} \boldsymbol{\psi}(\mathbf{a}[k]) \\ \mathbf{u}[k] \end{bmatrix}, \boldsymbol{\beta}[k] = \begin{bmatrix} \boldsymbol{\psi}(\mathbf{b}[k]) \\ \mathbf{u}[k] \end{bmatrix} \tag{11}$$

for each $k \in \{1, \ldots K\}$, the input $\mathbf{u}[k]$ is not lifted to ensure that the resulting model has linear input. With these discrete data pairs, the following $K \times (N + m)$ matrices are defined:

$$\mathbf{\Gamma}_\alpha = \begin{bmatrix} \boldsymbol{\alpha}[1]^T \\ \vdots \\ \boldsymbol{\alpha}[k]^T \end{bmatrix}, \mathbf{\Gamma}_\beta = \begin{bmatrix} \boldsymbol{\beta}[1]^T \\ \vdots \\ \boldsymbol{\beta}[k]^T \end{bmatrix} \tag{12}$$

and the Koopman operator could be calculated with (5)

$$\bar{\mathbf{\Omega}}_{T_s} := \mathbf{\Gamma}_\alpha^\dagger \mathbf{\Gamma}_\beta. \tag{13}$$

Note that by (5) and (13), the optimal approximation of the transition matrix could be obtained in the L^2-norm sense

$$\min_{\mathbf{\Omega}'} \sum_{k=1}^K \left\| \mathbf{\Omega}'^T \boldsymbol{\alpha}(k) - \boldsymbol{\beta}(k) \right\|_2^2 \tag{14}$$

and the $\mathbf{A} \in \mathbb{R}^{N \times N}$ and $\mathbf{B} \in \mathbb{R}^{N \times m}$ matrices satisfy the following:

$$\min_{\mathbf{A}',\mathbf{B}'} \sum_{k=1}^K \left\| \mathbf{A}'\boldsymbol{\psi}(\mathbf{a}[k]) + \mathbf{B}'\mathbf{u}[k] - \boldsymbol{\psi}(\mathbf{b}[k]) \right\|_2^2. \tag{15}$$

And the best $\mathbf{A}$ and $\mathbf{B}$ matrices of (10) can be obtained by partitioning $\bar{\mathbf{\Omega}}_{T_s}^T$ as follows:

$$\bar{\mathbf{\Omega}}_{T_s}^T = \begin{bmatrix} \mathbf{A}_{N \times N} & \mathbf{B}_{N \times m} \\ \mathbf{O}_{m \times N} & \mathbf{I}_{m \times m} \end{bmatrix} \tag{16}$$

where $\mathbf{I}_{m \times m}$ is an identity matrix, $\mathbf{O}_{m \times N}$ denotes a zero matrix, and the $\mathbf{C}$ matrix is defined as

$$\mathbf{C} = \begin{bmatrix} \mathbf{I}_{n \times n} & \mathbf{O}_{n \times (N-n)} \end{bmatrix}. \tag{17}$$

Thereby, a linear predictor has been determined with the discrete model form in (10).

2) Training Data Acquisition: The configuration parameters of the hydraulic-driven segment are defined as its bending direction and angle, with the inner pressures of three chamber adjusted by motor positions. The distal tendon-driven segment is controlled by altering tendon lengths, thus manipulating the bending direction φ and angle θ [Fig. 5(a)] of the laser lens. Data for identifying the linear model were collected by the randomized motion of the laser manipulator. For the tendon-driven segment, the tendon length could not be directly randomly adjusted due to the inherent structural constraint. Therefore, the training data were generated by randomly changing the parameters in the configuration space rather than that in the actuation space, as shown in Fig. 5(a). The bending angle θ and bending direction φ are randomly generated in the configuration space, with a predefined threshold to constraint the magnitude. In this article, we intend NOT to apply any pretension/load on the tendons, but propose to use spring as the backbone of tenson-driven mechanism, which store potential energy while bending. The
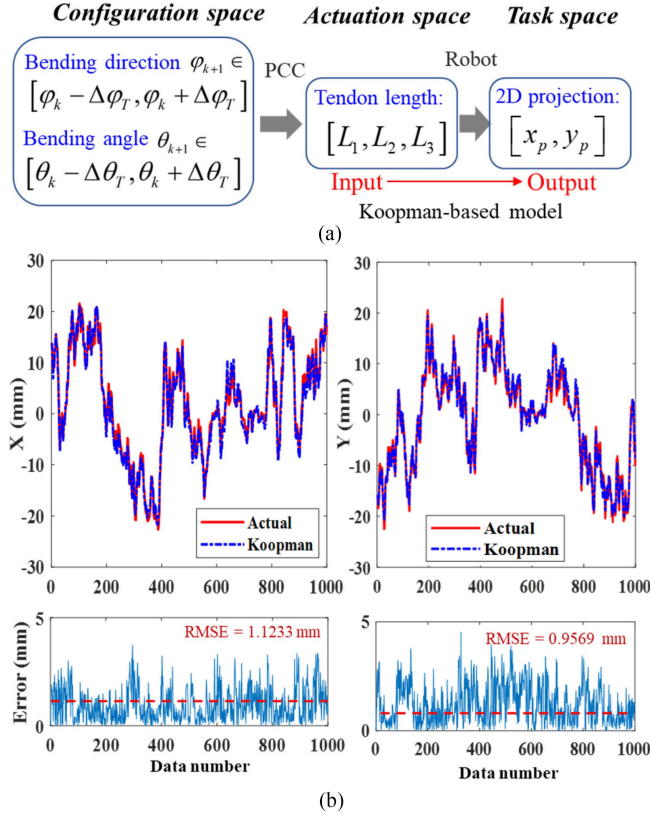
Fig. 5. Data collection and model validation for the Koopman-based model. (a) Data collection for model identification. The bending angle θ and bending direction φ were randomly initialized with a predefined threshold in the configuration space. (b) Validation of the data-driven model using Koopman theory. The predicted 2-D projection (in blue) are compared with the ground-truth (in red). The distance error is shown in the corresponding X- and Y-axis.

spring elasticity could restore the backbone to its natural shape rapidly, not requiring additional actuation to tense the slacked tendon, thus it could reduce the influence of slackness. Also, the data-driven method could resolve the remaining backlash issue by incorporating the nonlinear property into the model, as the training data would also cover the actuation status with slackness.

After collecting the data for the data-driven modeling approach, a Koopman-based linear model can be obtained, mapping from the tendon lengths to the 2-D projection position. The projection plane is perpendicular to the central axis of the robot. The 2-D projection position is calculated using the tip position and orientation, which are obtained by the real-time shape sensing feedback. A total of 15 000 pairs of data were used to identify the model, and another group of 1000 pairs (not involved in the training dataset) were utilized for validation. For the lift functions, fourth-order polynomials were chosen for its high prediction accuracy and low regression time, after comparing with other kinds of lift functions such as Gaussian and Fourier.

The accuracy of the data-driven model was validated by comparing with ground truth, as shown in Fig. 5(b). It is obvious that the predicted results match the true value well on both X

and Y dimensions, with small root mean square error (RMSE) of 1.1233 mm for the X direction and 0.9569 mm for the Y direction. These prediction results are promising compared with the motion range of the projection point ($\sim\pm23$ mm). Small errors were observed from the prediction results, which suggests that the data-driven model could approximate the real physical model accurately.

D. Disturbance-Observer for Closed-Loop Control

Disturbances and uncertainties are unavoidable in almost all robotic systems and bring negative effects on the control performance [44]. Therefore, rejecting or reducing disturbance and uncertainty are important in control system design, especially for surgical applications. For measurable disturbances, feed-forward strategies can be used to reduce or eliminate the influence. However, in most situations, the internal or external disturbances cannot be directly measured. A promising method to solve this problem is estimating the disturbance from measurable variables, followed by control strategies to reduce or eliminate the influence of disturbance. A similar strategy can be applied to deal with system uncertainties, by considering uncertainties or even unmodeled dynamics as a part of the disturbance.

In this article, a disturbance observer was designed to evaluate the model and sensing uncertainty, then used for compensation. The disturbance estimation $\hat{\mathbf{d}}$ is obtained by passing the modified output estimated error $\tilde{\mathbf{d}}$ through a low-pass filter $\mathbf{Q}_{\text{filter}}$, i.e.,

$$\hat{\mathbf{d}} = \mathbf{Q}_{\text{filter}}\tilde{\mathbf{d}}. \tag{18}$$

The modified estimation error of the output can be calculated with the least-squares solution given by the following equation:

$$\tilde{\mathbf{d}} = \mathbf{B}^{+}L\left(\mathbf{x} - \hat{\mathbf{x}}\right) + \hat{\mathbf{d}}. \tag{19}$$

With $\mathbf{B}^{+} = \left(\mathbf{B}^{T}\mathbf{B}\right)^{-1}\mathbf{B}^{T}$, and the gain L to be designed. When a low-pass filter is chosen for $\mathbf{Q}_{\text{filter}}$ as suggested in [60], it is as follows:

$$T_q\dot{\hat{\mathbf{d}}} + \hat{\mathbf{d}} = \tilde{\mathbf{d}}. \tag{20}$$

After involving (19), the equation can be rearranged as follows:

$$\dot{\hat{\mathbf{d}}} = \frac{1}{T_q}\mathbf{B}^{+}L\left(\mathbf{x} - \hat{\mathbf{x}}\right). \tag{21}$$

The estimated disturbance $\hat{\mathbf{d}}$ is determined by the difference between the measured output and its estimated value.

For the proposed robotic system, the controller design aims to find appropriate input tendon lengths which enable the laser projection point to follow a reference path. An overview of the control method is illustrated in Fig. 6. The multicore FBG fiber is utilized to provide real-time shape sensing for the continuum robot. The data-driven model uncertainty, the fiber shape sensing noise, and other uncertainty caused by tendon slackening, etc. are all treated as system uncertainty. A first-order low-pass filter is applied before the compensator is added into the main loop. The observer is designed by comparing the actual input and the estimated input via inverse kinematics. As a linear kinematic
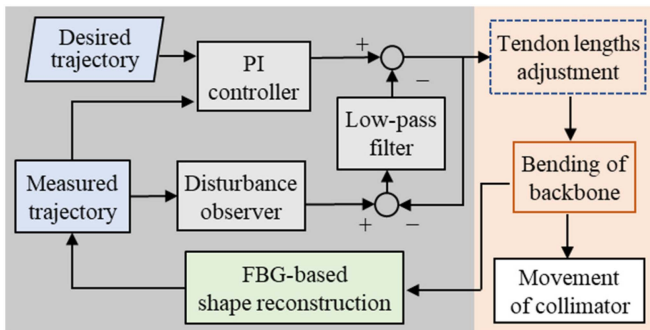
Fig. 6. Control schematic applied to the tendon-driven robot segment. Fiber optic shape sensing feeds back the pose of manipulator tip to both observer and controller. Disturbance-observer-based compensator is used to reduce the effect of model uncertainty and external disturbances, and the PI controller is to reduce tracking errors.

model has been identified in form of (10), the inverse kinematic can be obtained by direct inverse operation. In the proposed disturbance-observer-based controller, the PI component was selected to process the feedback and incorporate with the data-driven model. We implement it because of its wide applicability and simple tuning procedure. In this article, we prefer to use PI, skipping the derivative, D, under the PID control. The D (derivate) part usually works to counteract the rate of the state change, generally implemented in analog controllers. However, for our digital controller, the D part often results in oscillation because of the excessive settling time and rapid chattering along the desired path. With the D part as one of the feedback components, the slope of the control output relative to time would approach infinity and produce excessive volatile control signals.

The source of disturbance can come from external force and internal tendon friction, damping, and slackness during the tendon actuation. The external force applied when the robot segments is in contact with the lumen during the endoscopic navigation, the soft hydraulic-driven actuation could comply and adapt with the contacts with its lumen surrounding, and avoid damage to the soft tissues. As in our preliminary test [20] on the cadaver subject, the distal part of such a hydraulic-driven segment is usually rather free from the contacts, which can be steered toward the target laser ablation site by the use of close-loop controller with real-time sensing feedback. Furthermore, the tendon-driven mechanism is protected by outer shell from any external contact with soft tissue. To our observation, the disturbance to the tendon-driven mechanism mainly comes from the tendon slackness. Apart from the elasticity/spring property introduced to the mechanism, our proposed data-driven method also takes an important role to resolve the tendon-pulling backlash issue by incorporating the non-linear property into the model, as the training data would also include actuation status involving tendon slackness.

External force which is larger than the load capability (>0.4 N) would spoil the controller performance of the hydraulic-driven segment. Also, the controller cannot deal with high-frequency disturbance, i.e., beyond the bandwidth of the system (>1 Hz for the hydraulic-driven segment, and >10 Hz for
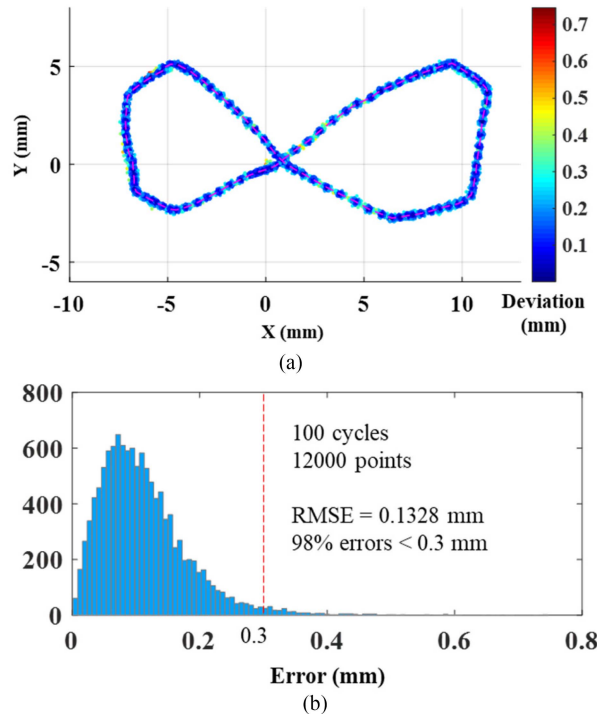

Fig. 7. Repeatability test of the tendon-driven segment. (a) Open-loop repeated scanning following an "∞" path over 100 cycles, with the colormap indicating the error. (b) Deviation distribution of the projection points, where most of the errors were less than 0.3 mm.

the tendon-drive segment). Increasing the robot stiffness could improve its dynamic response, thus enhancing the capability to deal with strong and high-frequency disturbance.

III. EXPERIMENT

A. Repeatability and Frequency Response

Aside from the controller design and performance, the actuator mechanical reliability is also of our concern. Despite the possibility for being used as a single-use device due to its low-cost 3-D printed design, adequate performance should be sufficiently maintained over its usage. The tendon-driven segment was first tested independently and controlled to follow an "∞" shape path with open-loop control repeatedly for 100 cycles [Fig. 7(a)]. The total operating time lasted approximately 1 h. The projection point moved following the path step-by-step, with the color indicating the deviation. The deviation distribution (compared with the mean value) is shown in Fig. 7(b), which shows that most of the errors (98%) were lower than 0.3 mm. This, to some degree, can reflect the repeatability of the manipulator.

The dynamic response of hydraulic soft manipulator and tendon-driven segment were both tested. For the long hydraulic segment, the soft chambers were pressured/released through hydraulic cylinders actuated by step motors. The robot tip position was captured with an EM tracking coil under periodic sinusoidal input with frequency ranging from 0.1 to 3 Hz. As shown in Fig. 8, the bandwidth of the hydraulic segment was about 0.75 Hz, at which frequency the magnitude decreased by 3 dB.
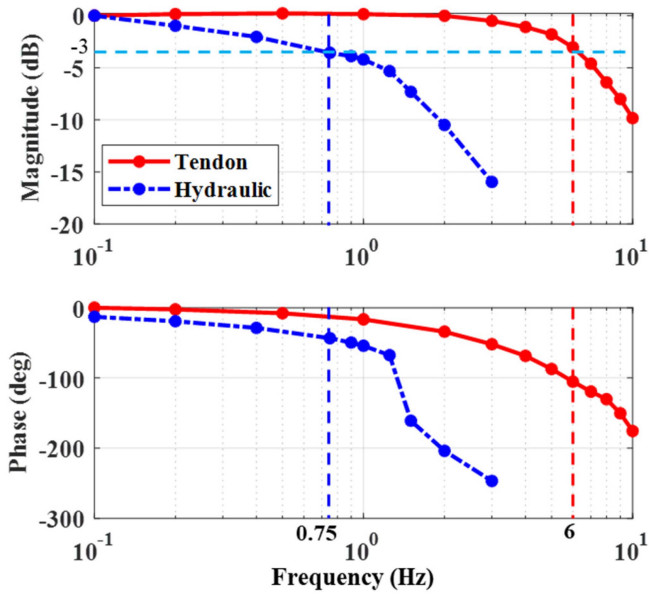
Fig. 8. Frequency response of each robot segment. The bandwidth was ~0.75 Hz for the hydraulic-driven segment and ~6 Hz for the tendon-driven segment. The cutoff frequencies were obtained where the magnitude response decreased by 3 dB.

This means that the adjusting frequency of the input commands should be less than 0.75 Hz, otherwise, they would be filtered by the soft robotic system. The same test was performed for the short tendon-driven segment, resulting in a measured bandwidth of approximately 6 Hz, which is much higher than that of the hydraulic segment. These results align with the original design that intends the hydraulic segment to be used for larger, slower bending, and the tendon-driven segment is for fast laser steering.

The hydraulic-driven segment comprises three reinforced soft chambers, where its dynamic response has great correlation with the density of spring partitions. In our previous article [20], finite-element analysis was used to analyze the bending stiffness of the spring reinforcements. Integrating multiple partitions of spring would help balance between the soft chamber dynamic response and durability. The distal segment is designed with a spring-tendon structure, where its dynamic characteristics are mainly determined by its spring backbone. In this article, closed-coil spring was chosen as the backbone of the tendon-driven segment. Either the mechanical parameters or material property would affect its dynamic response. As studies in our previous article, the increase in spring wire diameter has a quartic correlation with the bending stiffness [5]. Also, the spring made of stainless steel has a higher stiffness than nitinol. With the presence of a stiffer spring backbone, the tendon-driven mechanism could achieve higher operational frequencies. However, for the two-segment robot, there is a tradeoff to find a proper spring stiffness and ignore the coupling effect between the two segments.

B. Control Performance

With a kinematic model obtained with the Koopman-based method, the manipulator can be controlled to follow a reference
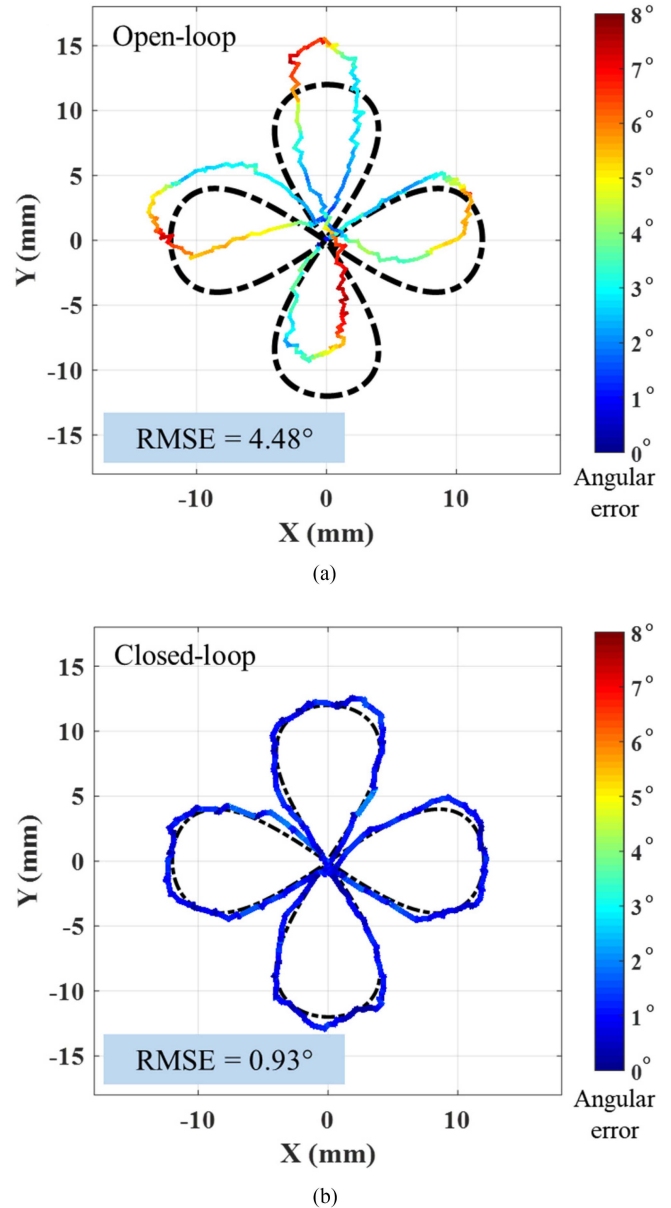

Fig. 9. Comparison of path following performance using (a) open-loop and (b) closed-loop control strategies demonstrated with a single path following cycle of a four-leaf pattern. The closed-loop controller could compensate for the modeling uncertainty, giving rise to the precision at RMSE = 0.93° only.

path. The control performance was evaluated by comparing open-loop and closed-loop control via a path following task performed over one tracking cycle. The control accuracies in Fig. 9 were initially measured as angular error of the laser lens with the colormap indicating the degree of error. For clarity, the errors could be interpreted as positional errors when projected onto the "ablation" plane. As shown in Fig. 9(a), the open-loop control method could roughly follow the path with large tracking errors with angular error of RMSE = 4.48° (RMSE: 2.53 mm with max. error: 5.13 mm). A bias toward the positive Y-axis could be seen, which could be accounted for by the data-driven model uncertainty and shape sensing noise. In comparison,
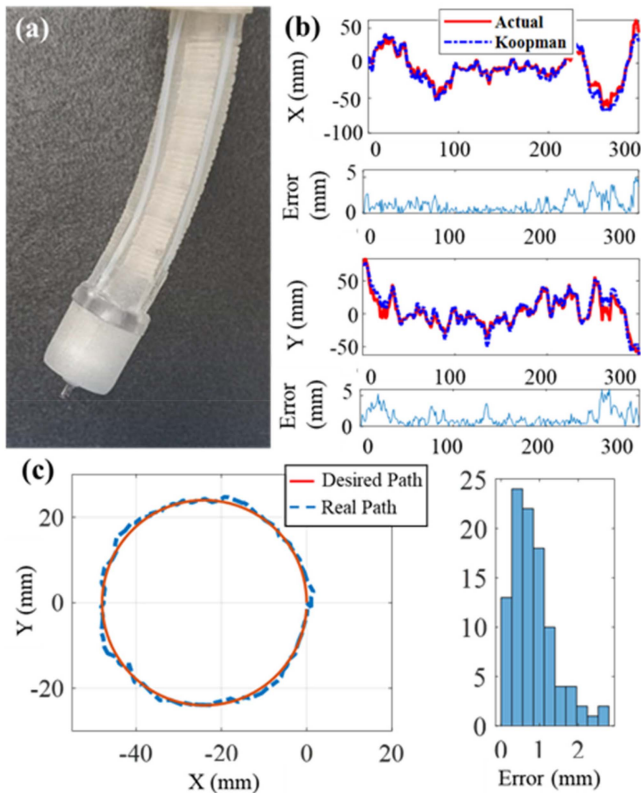
Fig. 10.   Performance of the proximal segment. (a) Bending direction and angle determined by the pressure of three soft chambers. (b) Validation of the data-driven model for the hydraulic segment using Koopman theory. (c) Control performance validation via path following with most of the errors <1.2 mm.

Fig. 11.   (a) Laser ablation configuration with collimator located ∼20 mm above the target ablation plane. (b) GRIN collimator integrated into the robot tip for laser ablation. (c) 3-D schematics of segment steering the collimator with three tendons. (d) Actual laser ablation on a foam board. Closed-loop control was applied to track the four-leaf pattern.

the closed-loop control method was able to follow the path more accurately with angular error of RMSE = 0.93° (RMSE: 0.634 mm with max. error: 1.65 mm), demonstrating substantial improvement.

Experiment has been performed to estimate the performance of the proximal segment, following a circular reference path. Fig. 10 shows the working performance of the hydraulic-driven segment, where the bending direction and angle are controlled by the liquid pressure of the three soft chambers. Fig. 10(b) shows the evaluation of the data-driven model compared with ground truth. Fig. 10(c) demonstrates the control performance by following the reference path, where >80% of the tracking errors were less than 1.2 mm.

C. Lab-Based Laser Ablation

As the aforementioned results and analysis were dependent on the calculated value obtained from optical fiber sensing data, some lab-based ablation experiments are performed to test the overall performance of the robotic system [Fig. 11(a)]. A GRIN lens [Fig. 11(b)] was inserted in the central channel of the robot with its tip fixed onto the distal end of the tendon-driven segment. The GRIN lens could emit a parallel-beam spot on the target and in combination with the robot's actuation, and can provide the ability to dexterously ablate tissue. For the ablation tests detailed below, the projection/target plane was positioned approximately
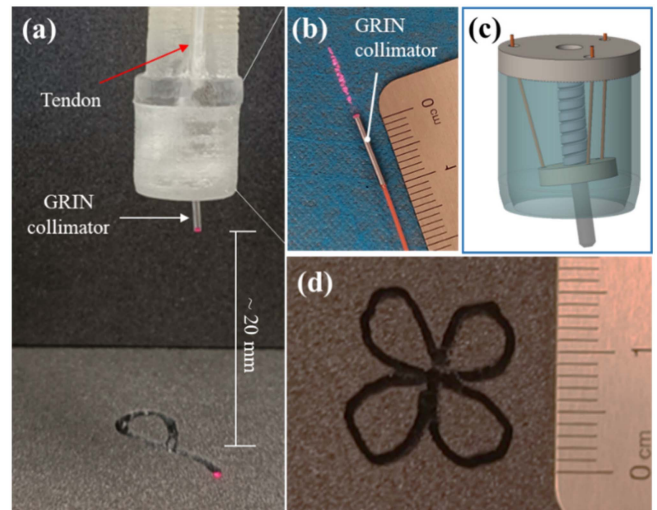
20 mm from the laser collimator tip, as shown in Fig. 11(a). A black foam board was used as the ablation surface to record the laser spot path, as shown in Fig. 11(d).

The laser ablation system was evaluated with the developed control strategy in further path following (Fig. 12). Three different patterns, i.e., a rectangle, spiral, and bat symbol, were used in the evaluation. The choice of the patterns aimed to cover various core components of complex paths, such as lines and right-angle turns in the rectangle, curved/circular paths in the spiral, and acute turns in bat-symbol pattern. For the rectangular pattern [Fig. 12(a) and (b)], larger errors occurred at the bottom and top corners, which are likely due to overshoot of PI controller, combined with the coupling effect of three tendons and their pretension status. Overall, the laser steerer demonstrated suitable precision for all three trajectories, with errors remaining <1 mm even for the more complex bat-symbol pattern.

D. Ex-Vivo Laser Ablation Test

The laser manipulation system and control strategy were also validated by a laser ablation test on *ex-vivo* pig tongue tissue [Fig. 13(b)]. A 1550 nm laser source was selected due to its high absorption rate in water. As seen from the Fig. 13, the laser ablation spot could accurately follow the predefined path, filling the desired boundary shape with RMSE = 0.384 mm. The "fish" ablation region could also be observed on the tissue surface, where the whole region was heated to a lighter color.

Thermal data (captured via a Fotric 222 s thermal camera) were also recorded to compare the open-loop control and closed-loop control with different sweeping speeds. A 1550 nm laser source (2.5 W) was chosen to project the laser on pig skin. Three types of ablation operation were performed and compared with fast scanning (7 s/cycle) and slow scanning (21 s/cycle) speeds. The three types of operations are: fast scanning with
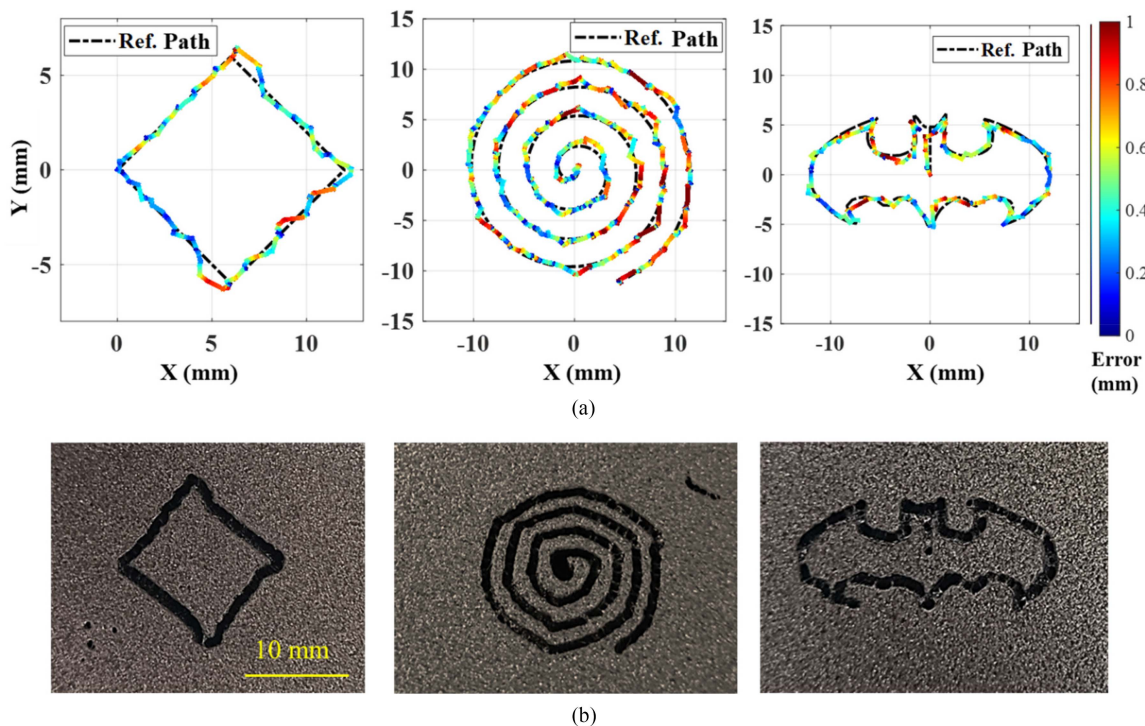
Fig. 12. Laser beam steering along three reference paths: a square, spiral, and bat symbol. (a) Tracking performed by the proposed control strategy. The colored lines indicate the actual path followed and the color temperature indicates the error compared to the reference path (dashed black line). (b) Corresponding laser "footprint" on the foam board in black.
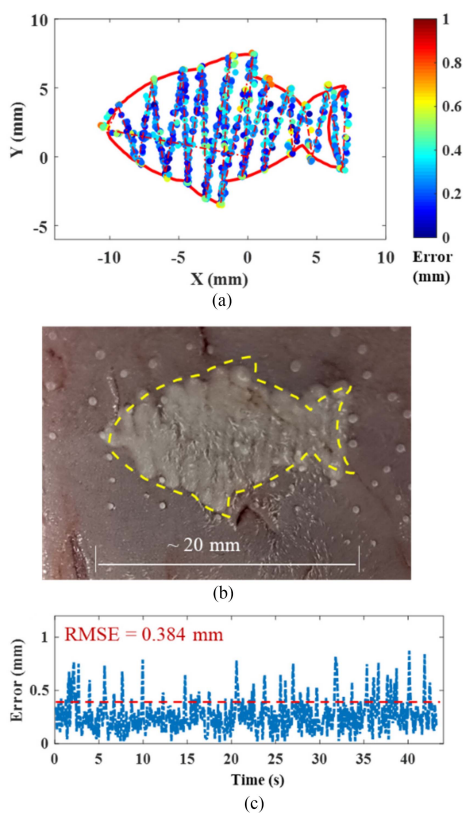
Fig. 13. Path following of a zig-zag pattern. (a) Laser spot steered to fill into a fish-shape contour. Warmer the color, higher the tracking error. (b) Corresponding ablation applied on *ex-vivo* pig tongue tissue.

Fig. 14. Thermal camera image of laser ablation on pigskin. Open- (first row) and closed-loop control (second/third row) are compared. Faster scanning mode with closed-loop control enables even distribution of heat. This would reduce the risk of excessive coagulation necrosis on *in-vivo* tissues.

Fig. 15. Tremor compensation carried out in (a) hand-held setting. Only tendon-driven segment is actuated, pointing the laser (red dot) toward a target point (yellow dot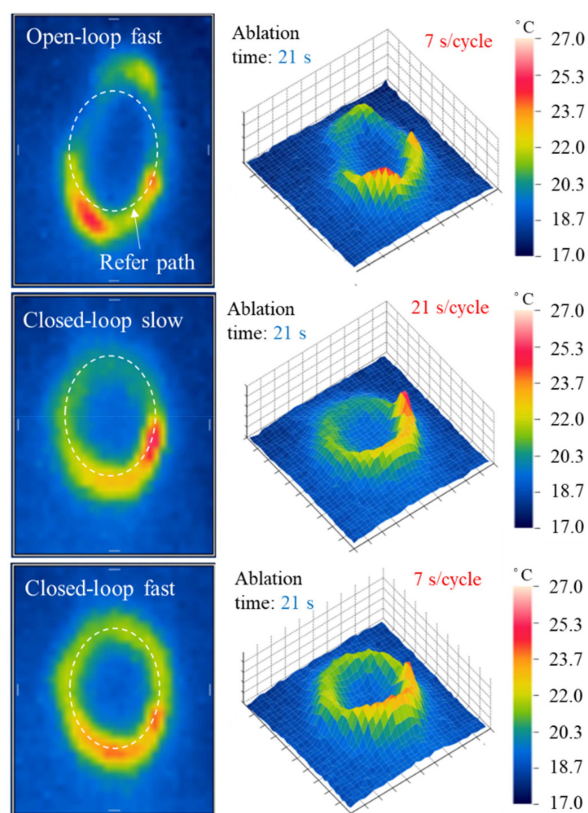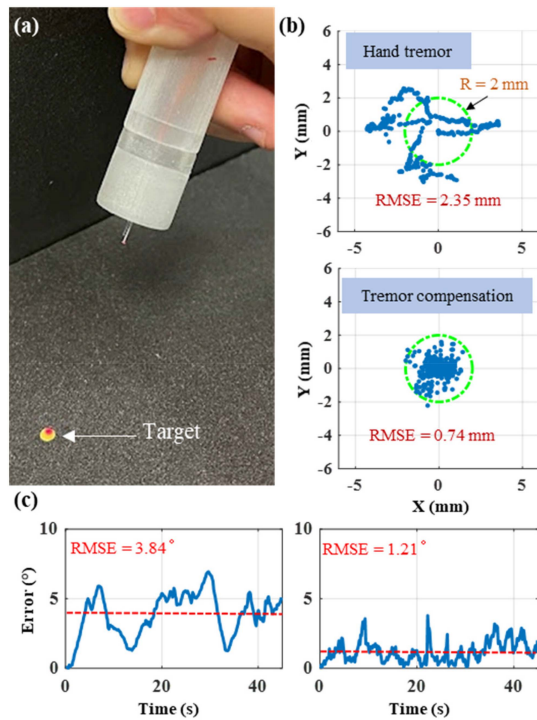). (b) Control performance comparison without/with tremor compensation. (c) Corresponding angular error plots with control accuracy improved from 3.84° to 1.21° RMSE.
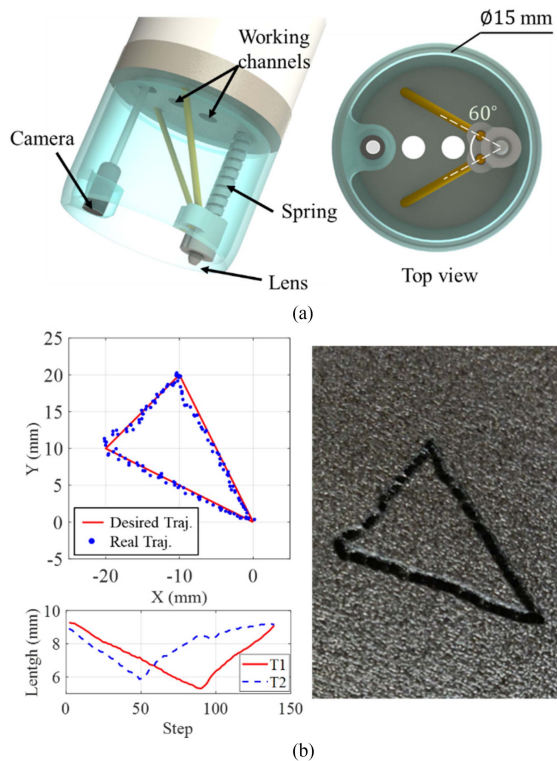

Fig. 16. Endoscopic application of the laser steering manipulator with two tendons. (a) Prototype of the unsymmetric spring-tendon structure, with a camera for visual feedback. (b) Laser beam steering along a triangle reference path driven by only two tendons, and the resultant ablation footprint on foam board.

open-loop control, slow scanning with closed-loop control, and fast scanning with closed-loop control. As shown in Fig. 14, the open-loop control (first row) could not follow the reference scanning path (a predefined circle) effectively, where obvious distortion was observed alongside uneven temperature distribution. With the closed-loop controller, both ablation trajectories in the slow and fast speeds could accurately follow the reference path. While the slow closed-loop scanning could reduce the local overheating compared with open-loop control, the fast closed-loop scanning could further improve the heating distribution, reducing hotspots caused by the natural bias of the robot and its modeling.

E. Tremor Compensation for Hand-Held Ablation

The fast-steering ability of the tendon-driven segment can also be used to compensate the hand tremor when used as a handheld device [61]. As shown in Fig. 15(a), the tendon-driven segment was used independently as part of a hand-held laser ablation device. The device was used to project the laser spot on the target, during which the physiological tremor may cause deviation. An EM coil was attached to the central channel of the device to measure its position and orientation, and was used to register the device to the EM field generator coordinate frame. Knowing the device's pointing direction, the deviation between the corresponding projected point on the ablation plane and the target spot could thus be measured. In combination with the optical fiber shape sensing feedback, the tendon-driven segment could compensate the error induced by hand tremor in real time. The EM tracking system (NDI, Aurora) has 40 Hz measurement rate, which is significantly higher than the tremor frequency 8–12 Hz as quoted. An EM positional marker capable of six-DoF pose measurement was integrated on the backend of handle (as shown in the picture below), and also coaxial with the FBG central channel. The hand-tremor amplitude could be around 50–100 μm peak to peak. Although this amplitude would be leveraged along the moment arm ($\sim$50 mm) of the hand-held device, by placing the EM marker at the backend, this translational amplitude would still be undetectable due to the limited EM 3-D-positional tracking resolution of 0.48 mm. However, this tremor-induced vibration, in terms of its angular amplitude, could be sufficiently large to be detected by the EM 3-D-orientational tracking with resolution of 0.30°. Fig. 15(b) and (c) shows the tendon-driven controller can substantially compensate the detectable tremor-induced vibration.

Results showing the effects of hand tremor without active robot compensation is shown in Fig. 15(b). The user's hand tremor would lead to large angular error of RMSE = 3.84° and max. error = 6.93° when focusing the laser spot (red) on the target point (yellow). With the compensation control strategy, the tracking error could be greatly improved, with RMSE 1.21° and maximum angular error around 3.79°. This corresponds to a positional error decrease from RMSE = 2.35 mm to 0.74 mm, allowing the laser to remain mostly within the target Ø 2 mm spot.

F. Endoscopic Laser Ablation With Unsymmetric Mechanism

In the previous sections, the data-driven method has been implemented on a hydraulic-driven segment and a tendon-driven segment, both of which has a symmetric mechanism. To further evaluate applicability of the Koopman-based method, an unsymmetric tendon-driven manipulator has been designed and tested. As shown in Fig. 16(a), an endoscopic tendon-driven prototype has been designed, with a unsymmetric structure using just two tendons. The camera fixed on the outer shell can provide the visual feedback for the ablation in real-time. Fig. 16(b) demonstrates the path following performance of the endoscopic laser ablation system and the real ablation effect on black foam board.

V. Conclusion

A two-segment compact robot is designed for flexible laser ablation. The long (56.4 mm) hydraulic-driven segment is composed of three spring reinforced chambers, enabling larger ($\sim$70°) and slower ($\sim$0.75 Hz) omnidirectional bending, relative to the steering motion of noncontact laser collimator centered at the short distal cap. The steering is actuated by three tendons with enhanced dynamics accredited to the designed spring backbone, as a result in fast and responsive ($\sim$6 Hz) laser steering. Such a two-segment prototype is compact (Ø12 mm) mostly for transoral endoscopic laser ablation. The design can be further downscaled as in our future article. However, our major work is to develop a data-driven control framework for a soft robotic laser manipulation system. Provided with the integration of OFDR-based FBG sensing, giving out high-frequency feedback of the robot shape and laser collimator pose in real time, our presented manipulation system becomes generic platform capable of incorporating with various control strategies.

Moreover, Koopman-operator-based modeling approach has been introduced, acting as a linear representation of the presented dynamic system. Uncertainty of the presented data-driven model can be compensated with the use of our disturbance observer. Together with the proposed controller, we have demonstrated rather precise laser path following across a variety of tests. For various scanning patterns, such as a four-leaf clover, spiral, bat symbol, as well as an irregular region filled with a zig-zag path, the tracking errors could be maintained below 1 mm even with proximity projection distance of $\sim$20 mm. The experiment results demonstrate the control performance of closed-loop control with PI control unit involved. The gains in the PI controller were fine-tuned based on any overshoot magnitude during the path following task. However, the drawback does exits. It can be observed that small deviation at the sharp path corners can still be found mostly due to the control overshoot, which is also considered as the limitation of such PI controller. To this end, investigation of variety of controllers (including model predictive control) will be a subject of our future article. Taking advantage of the tendon-driven mechanism, the manipulator can perform high velocity laser steering at around five times the speed of the hydraulic-driven manipulator presented in our previous article [20]. Applied in a hand-held setting, such high

tendon-driven steering speed is also sufficient to compensate hand tremor, and also to distribute thermal dose evenly, as results in less chance of coagulation necrosis formed on the *in-vivo* tissues. In this article, the backbone of the robot is a metal spring fabricated from a nitinol tube using laser cutting. The robot has showed stable sweeping performance after over 20 h ablation tasks with coverage of most of its workspace, which is attributed to the great repeatability and durability of the nitinol spring.

By far, only FBG-based shape sensing is utilized as feedback to close the control loop. Visual camera could be also another self-contained sensing add-on providing additional real-time feedback by visually tracking the laser spot in the camera view. Visible light could be emitted through the same laser fiber to project a visible laser spot which can be tracked with feature detection algorithms. The vision-based laser spot measurement, along with the FBG-based shape sensing, can be fused to further improve the control performance. Again, it will avoid reliance on the use of external positional tracking devices, such as EM tracking. Potential applications include ablative laser resurfacing or tattoo removal, where the laser targeting needs to be rapid and automatic for effective laser sweeping on skin, even in hand-held operation setting.

References

[1] J. Burgner-Kahrs, D. C. Rucker, and H. Choset, "Continuum robots for medical applications: A survey," *IEEE Trans. Robot.*, vol. 31, no. 6, pp. 1261–1280, Dec. 2015.

[2] C. Shi et al., "Shape sensing techniques for continuum robots in minimally invasive surgery: A survey," *IEEE Trans. Biomed. Eng.*, vol. 64, no. 8, pp. 1665–1678, Aug. 2017.

[3] H. B. Gilbert, D. C. Rucker, and R. J. Webster, III, "Concentric tube robots: The state of the art and future directions," in *Robotics Research*. Berlin, Germany: Springer, 2016, pp. 253–269.

[4] V. Vitiello, K.-W. Kwok, and G.-Z. Yang, "Introduction to robot-assisted minimally invasive surgery (MIS)," in *Medical Robotics*. Amsterdam, The Netherlands: Elsevier, 2012, pp. 1–P1.

[5] H.-C. Fu et al., "Interfacing soft and hard: A spring reinforced actuator," *Soft Robot.*, vol. 7, no. 1, pp. 44–58, 2020.

[6] Z. Guo et al., "Compact design of a hydraulic driving robot for intraoperative MRI-guided bilateral stereotactic neurosurgery," *IEEE Robot. Automat. Lett.*, vol. 3, no. 3, pp. 2515–2522, Jul. 2018.

[7] P. Gomes, "Surgical robotics: Reviewing the past, analysing the present, imagining the future," *Robot. Comput.-Integr. Manuf.*, vol. 27, no. 2, pp. 261–266, 2011.

[8] B. S. Peters, P. R. Armijo, C. Krause, S. A. Choudhury, and D. Oleynikov, "Review of emerging surgical robotic technology," *Surg. Endoscopy*, vol. 32, no. 4, pp. 1636–1655, 2018.

[9] D. Kundrat et al., "Toward assistive technologies for focus adjustment in teleoperated robotic non-contact laser surgery," *IEEE Trans. Med. Robot. Bionics*, vol. 1, no. 3, pp. 145–157, Aug. 2019.

[10] E. Schena, P. Saccomandi, and Y. Fong, "Laser ablation for cancer: Past, present and future," *J. Funct. Biomater.*, vol. 8, no. 2, 2017, Art. no. 19.

[11] W. T. Latt et al., "A hand-held instrument for in vivo probe-based confocal laser endomicroscopy during minimally invasive surgery," in *Proc. IEEE/RSJ Int. Conf. Intell. Robots Syst.*, 2012, pp. 1982–1987.

[12] E. C. Kauffman, H. W. Kang, and B. B. Choi, "The effect of laser-fiber sweeping speed on the efficiency of photoselective vaporization of the prostate in an ex vivo bovine model," *J. Endourol.*, vol. 23, no. 9, pp. 1429–1435, 2009.

[13] J. Oh, S. Y. Nam, Y. W. Lee, and H. W. Kang, "Effect of multiple-sweeping on ablation performance during ex vivo laser nephrectomy," *Lasers Surg. Med.*, vol. 48, no. 6, pp. 616–623, 2016.

[14] R. Renevier, B. Tamadazte, K. Rabenorosoa, L. Tavernier, and N. Andreff, "Endoscopic laser surgery: Design, modeling, and control," *IEEE/ASME Trans. Mechatron.*, vol. 22, no. 1, pp. 99–106, Feb. 2017.

[15] M. Zhao, T. J. O. Vrielink, A. A. Kogkas, M. S. Runciman, D. S. Elson, and G. P. Mylonas, "LaryngoTORS: A novel cable-driven parallel robotic system for transoral laser phonosurgery," *IEEE Robot. Automat. Lett.*, vol. 5, no. 2, pp. 1516–1523, Apr. 2020.

[16] M. Rubinstein and W. B. Armstrong, "Transoral laser microsurgery for laryngeal cancer: A primer and review of laser dosimetry," *Lasers Med. Sci.*, vol. 26, no. 1, pp. 113–124, 2011.

[17] M. Remacle, G. Lawson, M.-C. Nollevaux, and M. Delos, "Current state of scanning micromanipulator applications with the carbon dioxide laser," *Ann. Otol. Rhinol. Laryngol.*, vol. 117, no. 4, pp. 239–244, 2008.

[18] A. Acemoglu, N. Deshpande, and L. S. Mattos, "Towards a magnetically-actuated laser scanner for endoscopic microsurgeries," *J. Med. Robot. Res.*, vol. 3, no. 2, 2018, Art. no. 1840004.

[19] S. Patel, M. Rajadhyaksha, S. Kirov, Y. Li, and R. Toledo-Crow, "Endoscopic laser scalpel for head and neck cancer surgery," in *Proc. Photonic Therapeutics Diagnostics VIII*, 2012, pp. 82071S.

[20] G. Fang et al., "Soft robotic manipulator for intraoperative MRI-guided transoral laser microsurgery," *Sci. Robot.*, vol. 6, no. 57, 2021, Art. no. eabg5575.

[21] Y. Hu, L. Zhang, W. Li, and G.-Z. Yang, "Design and fabrication of a 3-D printed metallic flexible joint for snake-like surgical robot," *IEEE Robot. Automat. Lett.*, vol. 4, no. 2, pp. 1557–1563, Apr. 2019.

[22] R. J. Webster, III and B. A. Jones, "Design and kinematic modeling of constant curvature continuum robots: A review," *Int. J. Robot. Res.*, vol. 29, no. 13, pp. 1661–1683, 2010.

[23] K. Xu and N. Simaan, "Analytic formulation for kinematics, statics, and shape restoration of multibackbone continuum robots via elliptic integrals," *J. Mech. Robot.*, vol. 2, no. 1, 2010, Art. no. 011006.

[24] E. Lugez, H. Sadjadi, D. R. Pichora, R. E. Ellis, S. G. Akl, and G. Fichtinger, "Electromagnetic tracking in surgical and interventional environments: Usability study," *Int. J. Comput. Assist. Radiol. Surg.*, vol. 10, no. 3, pp. 253–262, 2015.

[25] K.-H. Lee et al., "Nonparametric online learning control for soft continuum robot: An enabling technique for effective endoscopic navigation," *Soft Robot.*, vol. 4, no. 4, pp. 324–337, 2017.

[26] A. M. Franz, T. Haidegger, W. Birkfellner, K. Cleary, T. M. Peters, and L. Maier-Hein, "Electromagnetic tracking in medicine—A review of technology, validation, and applications," *IEEE Trans. Med. Imag.*, vol. 33, no. 8, pp. 1702–1725, Aug. 2014.

[27] H. Zhao, J. Jalving, R. Huang, R. Knepper, A. Ruina, and R. Shepherd, "A helping hand: Soft orthosis with integrated optical strain sensors and EMG control," *IEEE Robot. Automat. Mag.*, vol. 23, no. 3, pp. 55–64, Sep. 2016.

[28] C. K. Harnett, H. Zhao, and R. F. Shepherd, "Stretchable optical fibers: Threads for strain-sensitive textiles," *Adv. Mater. Technol.*, vol. 2, no. 9, 2017, Art. no. 1700087.

[29] P. Wei, J. Liu, Z. Dai, and M. Li, "Monitoring the shape of satellite wing frame using FBG sensors in high electronic noise, vacuum, and −196°C environment," *IEEE Trans. Ind. Electron.*, vol. 64, no. 1, pp. 691–700, Jan. 2017.

[30] K. O. Hill and G. Meltz, "Fiber Bragg grating technology fundamentals and overview," *J. Lightw. Technol.*, vol. 15, no. 8, pp. 1263–1276, Aug. 1997.

[31] H. Wang, R. Zhang, W. Chen, X. Liang, and R. Pfeifer, "Shape detection algorithm for soft manipulator based on fiber Bragg gratings," *IEEE/ASME Trans. Mechatron.*, vol. 21, no. 6, pp. 2977–2982, Dec. 2016.

[32] K. R. Henken, J. Dankelman, J. J. van den Dobbelsteen, L. K. Cheng, and M. S. van der Heiden, "Error analysis of FBG-based shape sensors for medical needle tracking," *IEEE/ASME Trans. Mechatron.*, vol. 19, no. 5, pp. 1523–1531, Oct. 2014.

[33] T. L. T. Lun, K. Wang, J. D. Ho, K.-H. Lee, K. Y. Sze, and K.-W. Kwok, "Real-time surface shape sensing for soft and flexible structures using fiber Bragg gratings," *IEEE Robot. Automat. Lett.*, vol. 4, no. 2, pp. 1454–1461, Apr. 2019.

[34] K. Wang et al., "Large-scale surface shape sensing with learning-based computational mechanics," *Adv. Intell. Syst.*, vol. 3, no. 11, 2021, Art. no. 2100089.

[35] M. Amanzadeh, S. M. Aminossadati, M. S. Kizil, and A. D. Rakić, "Recent developments in fibre optic shape sensing," *Measurement*, vol. 128, pp. 119–137, 2018.

[36] Z. Dong et al., "Shape tracking and feedback control of cardiac catheter using MRI-guided robotic platform–Validation with pulmonary vein isolation simulator in MRI," *IEEE Trans. Robot.*, vol. 38, no. 5, pp. 2781–2798, Oct. 2022.

[37] X. Wang, Y. Li, and K.-W. Kwok, "A survey for machine learning-based control of continuum robots," *Front. Robot. AI*, vol. 280, pp. 1–14, 2021.

[38] D. Kim et al., "Review of machine learning methods in soft robotics," *Plos One*, vol. 16, no. 2, 2021, Art. no. e0246102.

[39] X. Wang et al., "Eye-in-hand visual servoing enhanced with sparse strain measurement for soft continuum robots," *IEEE Robot. Automat. Lett.*, vol. 5, no. 2, pp. 2161–2168, Apr. 2020.

[40] D. Bruder, X. Fu, R. B. Gillespie, C. D. Remy, and R. Vasudevan, "Data-driven control of soft robots using Koopman operator theory," *IEEE Trans. Robot.*, vol. 37, no. 3, pp. 948–961, Jun. 2021.

[41] D. Bruder, X. Fu, and R. Vasudevan, "Advantages of bilinear Koopman realizations for the modeling and control of systems with unknown dynamics," *IEEE Robot. Automat. Lett.*, vol. 6, no. 3, pp. 4369–4376, Jul. 2021.

[42] D. Arnas and R. Linares, "Approximate analytical solution to the zonal harmonics problem using Koopman operator theory," *J. Guid. Control Dyn.*, vol. 44, no. 11, pp. 1909–1923, 2021.

[43] D. Bruder, C. D. Remy, and R. Vasudevan, "Nonlinear system identification of soft robot dynamics using Koopman operator theory," in *Proc. IEEE Int. Conf. Robot. Automat.*, 2019, pp. 6244–6250.

[44] W.-H. Chen, J. Yang, L. Guo, and S. Li, "Disturbance-observer-based control and related methods—An overview," *IEEE Trans. Ind. Electron.*, vol. 63, no. 2, pp. 1083–1095, Feb. 2016.

[45] E. Sariyildiz, R. Oboe, and K. Ohnishi, "Disturbance observer-based robust control and its applications: 35th anniversary overview," *IEEE Trans. Ind. Electron.*, vol. 67, no. 3, pp. 2042–2053, Mar. 2020.

[46] N. Simaan, R. Taylor, and P. Flint, "A dexterous system for laryngeal surgery," in *Proc. IEEE Int. Conf. Robot. Automat.*, 2004, pp. 351–357.

[47] S. C. Ryu et al., "Design of an optically controlled MR-compatible active needle," *IEEE Trans. Robot.*, vol. 31, no. 1, pp. 1–11, Feb. 2014.

[48] N. J. van de Berg, J. Dankelman, and J. J. van den Dobbelsteen, "Design of an actively controlled steerable needle with tendon actuation and FBG-based shape sensing," *Med. Eng. Phys.*, vol. 37, no. 6, pp. 617–622, 2015.

[49] K. Mandal, F. Parent, S. Martel, R. Kashyap, and S. Kadoury, "Vessel-based registration of an optical shape sensing catheter for MR navigation," *Int. J. Comput. Assist. Radiol. Surg.*, vol. 11, no. 6, pp. 1025–1034, 2016.

[50] T. Li, C. Shi, and H. Ren, "Three-dimensional catheter distal force sensing for cardiac ablation based on fiber bragg grating," *IEEE/ASME Trans. Mechatron.*, vol. 23, no. 5, pp. 2316–2327, Oct. 2018.

[51] Z. Tang, S. Wang, M. Li, and C. Shi, "Development of a distal tri-axial force sensor for minimally invasive surgical palpation," *IEEE Trans. Med. Robot. Bionics*, vol. 4, no. 1, pp. 145–155, Feb. 2022.

[52] G. Flockhart, W. MacPherson, J. Barton, J. Jones, L. Zhang, and I. Bennion, "Two-axis bend measurement with Bragg gratings in multicore optical fiber," *Opt. Lett.*, vol. 28, no. 6, pp. 387–389, 2003.

[53] B. Childlers, D. Gifford, R. Duncan, M. Raum, and M. Vercellino, "Fiber optic position and shape sensing device and method relating thereto," U.S. Patent US7781724B2, 2006.

[54] J. P. Moore and M. D. Rogge, "Shape sensing using multi-core fiber optic cable and parametric curve solutions," *Opt. Exp.*, vol. 20, no. 3, pp. 2967–2973, 2012.

[55] M. D. Rogge and J. P. Moore, "Shape sensing using a multi-core optical fiber having an arbitrary initial shape in the presence of extrinsic forces," U.S. Patent 8,746,076, Jun. 10, 2014.

[56] D. Kundrat et al., "Preclinical performance evaluation of a robotic endoscope for non-contact laser surgery," *Ann. Biomed. Eng.*, vol. 49, no. 2, pp. 585–600, 2021.

[57] A. Mauroy and J. Goncalves, "Koopman-based lifting techniques for nonlinear systems identification," *IEEE Trans. Autom. Control*, vol. 65, no. 6, pp. 2550–2565, Jun. 2019.

[58] A. Mauroy and J. Goncalves, "Linear identification of nonlinear systems: A lifting technique based on the Koopman operator," in *Proc. IEEE 55th Conf. Decis. Control*, 2016, pp. 6500–6505.

[59] R. Penrose, "On best approximate solutions of linear matrix equations," *Math. Proc. Cambridge Philos. Soc.*, vol. 52, no. 1, pp. 17–19, 1956.

[60] J.-H. She, X. Xin, and Y. Pan, "Equivalent-input-disturbance approach—Analysis and application to disturbance rejection in dual-stage feed drive control system," *IEEE/ASME Trans. Mechatron.*, vol. 16, no. 2, pp. 330–340, Apr. 2011.

[61] C. J. Payne, K.-W. Kwok, and G.-Z. Yang, "An ungrounded hand-held surgical device incorporating active constraints with force-feedback," in *Proc. IEEE/RSJ Int. Conf. Intell. Robots Syst.*, 2013, pp. 2559–2565.

Kui Wang received the B.E. degree in automation and the M.E. degree in control science and engineering from the Nankai University, Tianjin, China, in 2013 and 2016, respectively, and the Ph.D. degree in robotics from The University of Hong Kong, Hong Kong, in 2022.

His research interests include flexible shape sensing, soft robotic system, and data-driven robot control.

Xiaomei Wang received the B.E. degree in automation from the Harbin Institute of Technology, Harbin, China, in 2014, the M.E. degree in control science and engineering from the Shenzhen Graduate School, Harbin Institute of Technology, Shenzhen, China, in 2016, and the Ph.D. degree in robotics from The University of Hong Kong, Hong Kong, in 2020.

She is currently a Postdoctoral Fellow with the Department of Mechanical Engineering, University of Hong Kong. Her research interests include learning-based robot control and sensing, surgical robotics, and continuum robot control.

Dr. Wang serves as an Associate Editor for ICRA 2022–2023 and RoboSoft 2022–2023, and an Area Chair for IPCAI 2022.

Justin Di-Lang Ho received the bachelor's degree in mechatronic engineering from The University of Queensland, Brisbane, QLD, Australia, in 2016, and the M.Phil. degree in the field of robotics from the Department of Mechanical Engineering, The University of Hong Kong, Hong Kong, in 2019.

His research interests include minimally invasive surgical robotics, including MRI-guided robotics and miniaturized robotic instruments.

Ge Fang received the bachelor's degree in mechanical engineering from the Huazhong University of Science and Technology, Wuhan, China, in 2014, the master's degree from the Shanghai Jiao Tong University, Shanghai, China, in 2017, and the Ph.D. degree in robotics from The University of Hong Kong, Hong Kong, in 2021.

His research interests include magnetic resonance imaging-guided robotics system, soft robotics, and learning-based robot control.

Bohao Zhu received the B.E. degree in automation from the Harbin Institute of Technology, Harbin, China, in 2015, and the Ph.D. degree in control theory from The University of Hong Kong (HKU), Hong Kong, in 2020.

From 2020 to 2021, he worked with The Chinese University of Hong Kong, Hong Kong, as a Research Associate. He is currently a Postdoctoral Fellow with the Department of Mechanical Engineering, HKU. His research interests include periodic systems, positive systems, optimal control, and robotic systems.

Rongying Xie received the bachelor's degree in mechanical engineering and automation from the Guangzhou College of South China University of Technology, Guangzhou, China, in 2014, and the master's degree in mechanical engineering from The University of Hong Kong, Hong Kong, in 2020.

Yun-Hui Liu (Fellow, IEEE) received the B.Eng. degree in applied dynamics from the Beijing Institute of Technology, Beijing, China, in 1985, the M.Eng. degree in mechanical engineering from the Osaka University, Suita, Japan, in 1989, and the Ph.D. degree in mathematical engineering and information physics from the University of Tokyo, Tokyo, Japan, in 1992.

He is currently a Choh-Ming Li Professor of mechanical and automation engineering with the Faculty of Engineering, The Chinese University of Hong Kong, Hong Kong. He is also an Adjunct Professor with the State Key Laboratory of Robotics Technology and System, Harbin Institute of Technology, Harbin, China; a ChangJiang Professor with the National University of Defense Technology (NUDT), Changsha, China, and a Visiting Professor with the Beijing Institute of Technology, Beijing, China. He is the Director of CUHK T Stone Robotics Institute and the Director of the Joint Center for Intelligent Sensing and Systems of CUHK and NUDT. He also serves as the Director/CEO of the Hong Kong Centre for Logistics Robotics, Hong Kong, sponsored by the InnoHK Programme of the HKSAR Government. He has authored/coauthored more than 500 papers in refereed journals and refereed conference proceedings. He was listed in the Highly Cited Authors (Engineering) by Thomson Reuters in 2013. His research interests include visual servoing, logistics robotics, medical robotics, multifingered grasping, mobile robots, and machine intelligence.

Prof. Liu was the recipient of numerous research awards from international journals and international conferences in robotics and automation, and government agencies. He has served as the General Chair of the 2006 IEEE/RSJ International Conference on Intelligent Robots and Systems. He has served as an Associate Editor for the IEEE TRANSACTIONS ON ROBOTICS AND AUTOMATION. He was the Editor-in-Chief of Robotics and Biomimetics.

Kwok Wai Samuel Au received the B.Eng. and M.Phil degrees in mechanical and automation engineering from The Chinese University of Hong Kong (CUHK), Hong Kong, China, in 1997 and 1999, respectively, and the Ph.D. degree in mechanical engineering from the Massachusetts Institute of Technology (MIT), Cambridge, MA, USA, in 2007.

Prof. Hugh Herr, Dr. Au, and other colleagues from the MIT Biomechatronics group coinvented the MIT Powered Ankle-foot Prosthesis. This invention was later commercialized by iWalk, Inc. He is currently a Professor with the Department of Mechanical and Automation Engineering and Department of Surgery (by courtesy), CUHK. He is also the Founding Co-Director of the Multiscale Medical Robotics Center of InnoHK Research Cluster. Before joining CUHK (2016), he was the Manager of Systems Analysis of the New Product Development Department at Intuitive Surgical, Inc. at Intuitive Surgical, he coinvented and was leading the software and control algorithm development for the FDA cleared da Vinci Si Single-Site surgical platform (2012), Single-Site Wristed Needle Driver (2014), and da Vinci Xi Single-Site surgical platform (2016). Since the official launch in Dec. 2012, more than 100K patients have received the single incision surgery through this platform. He was also a founding team member for the early development of Intuitive Surgical's FDA cleared robot-assisted catheter system, da Vinci ION system from 2008 to 2012. He has coauthored more than 48 peer-reviewed manuscripts and conference journals, 17 granted U.S. patents/EP, and 3 pending U.S. Patents.

Prof. Au was the recipient of numerous awards including the first prize in the American Society of Mechanical Engineers Student Mechanism Design Competition in 2007, Intuitive Surgical Problem Solving Award in 2010, and Intuitive Surgical Inventor Award in 2011.

Jason Ying-Kuen Chan received the graduate degree in medicine from the Guy's, King's and St. Thomas' School of Medicine in London, London, U.K., in July 2005, followed by completion of specialist training in Otolaryngology, Head and Neck surgery from the the Johns Hopkins School of Medicine with advanced training in head and neck surgery on microvascular reconstruction and robotics, in June 2013.

He has been with the Department of Otorhinolaryngology, Head & Neck Surgery, The Chinese University of Hong Kong, Hing Kong, since September 2014, and is currently an Associate professor with the department. He was involved in the initial human clinical trial of the *da Vinci SP* in transoral robotic surgery. He has authored/coauthored more than 110 publications. His research interests include the microbiome, diagnosis, treatment, and surveillance of head and neck cancers and the development of novel robotic applications for head and neck surgery.

Mr. Chan is currently an Associate Editor for the *Journal of Otolaryngology, Head and Neck Surgery* (Rank 5/43 in Otorhinolaryngology). He also acts as a Chairman of the Head and Neck Surgery Board, Hong Kong College of Otorhinolaryngologists, Hong Kong. His qualifications include Licentiate of Medical Council of Hong Kong, Bachelor of Medicine and Bachelor of Surgery (London), Diplomate American Board of Otolaryngology, Head and Neck Surgery, Fellow of the Hong Kong College of Otorhinolaryngology, Fellow of the Hong Kong Academy of Medicine (Otorhinolaryngology), and Fellow of the Royal College of Surgeons Edinburgh (Otolaryngology).

Ka-Wai Kwok (Senior Member, IEEE) received the B.Eng. and M.Phil. degrees in automation and computer-aided engineering from The Chinese University of Hong Kong, Hong Kong, in 2003 and 2005, respectively, and the Ph.D. degree in computing from the Hamlyn Center for Robotic Surgery, Department of Computing, Imperial College London, London, U.K., in 2012.

He is currently an Associate Professor with the Department of Mechanical Engineering, University of Hong Kong (HKU), Hong Kong. Prior to joining HKU, in 2014, he worked as a Postdoctoral Fellow with the Imperial College London, in 2012, for surgical robotics research. In 2013, he was awarded the Croucher Foundation Fellowship, which supported his research jointly supervised by advisors from the University of Georgia, Athens, GA, USA, and Brigham and Women's Hospital, Harvard Medical School, Boston, MA, USA. He has coauthored more than 140 publications with more than 50 clinical fellows and more than 90 engineering scientists, and 6 out of 14 invention patents licensed/transferred to industrial partners in support for their commercialization. His research interests include surgical robotics, intraoperative image processing, and their uses of intelligent and control systems.

Dr. Kwok was the recipient of more than 10 international publication awards, mostly under IEEE, particularly in the largest flagship conferences of robotics: e.g., ICRA Best Conference Paper Award in 2018, and IROS Toshio Fukuda Young Professional Award in 2020. He also serves as an Associate Editor for *Journal of Systems and Control Engineering*, IEEE ROBOTICS AND AUTOMATION MAGAZINE, and *Annals of Biomedical Engineering*. He is the Principal Investigator of research group for Interventional Robotic and Imaging Systems, HKU.